CRYSTAL GROWTH & DESIGN

pubs.acs.org/crystal

Article

Isomorphous but No Dead Ringer: Contrasting the Supramolecular Binding of Tetrafluoroberyllate and Sulfate Ions by Nanojars

Wisam A. Al Isawi, Matthias Zeller, and Gellert Mezei*

Cite This: *Cryst. Growth Des.* 2023, 23, 1676−1688

Read Online

ACCESS | Metrics & More | Article Recommendations | Supporting Information

Downloaded via WESTERN MICHIGAN UNIV on March 1, 2023 at 21:56:09 (UTC).
See https://pubs.acs.org/sharingguidelines for options on how to legitimately share published articles.

ABSTRACT: An extensive single-crystal X-ray crystallographic study of 11 nanojar structures (of which seven are novel) of the formula [anion⊂{*cis*-$Cu^{II}(\mu\text{-OH})(\mu\text{-pz})\}_n]^{2-}$ (anion = BeF_4^{2-}, n = 28, 31, 32, Cu_nBeF_4; anion = SO_4^{2-}, n = 28, 31, Cu_nSO_4; pz = pyrazolate, $C_3H_3N_2^-$) has been carried out, providing a detailed description of isomorphism and pseudopolymorphism in nanojars. The results point to a remarkable variety in the shape of the constituent $[cis\text{-}Cu^{II}(\mu\text{-OH})(\mu\text{-pz})]_x$ (Cu_x; x = 6, 8, 9, 10, 12 and 14) metallamacrocycles, despite only small differences in the coordination environment of the individual Cu^{2+} centers. The flexibility of the Cu_x rings and, ultimately, of the nanojar framework allows for the incarceration of different anions with slightly different dimensions in a nanojar of a given size, resulting in the formation of isomorphous structures in the case of Cu_nBeF_4 and Cu_nSO_4. Selectivity studies monitored by electrospray-ionization mass spectrometry (ESI-MS) and proton nuclear magnetic resonance spectroscopy (^{1}H NMR) reveal that despite the virtually identical H-bonding pattern around the two anions in nanojars of a given size, SO_4^{2-} is strongly preferred over BeF_4^{2-}. The origins of this selectivity are discussed, along with the nature of bonding in the two isosteric anions. Lastly, the crystal structure of $(Bu_4N)_3Be_2F_7(H_2O)_3$ documents the formation of the $Be_2F_7^{3-}$ ion from BeF_4^{2-}.

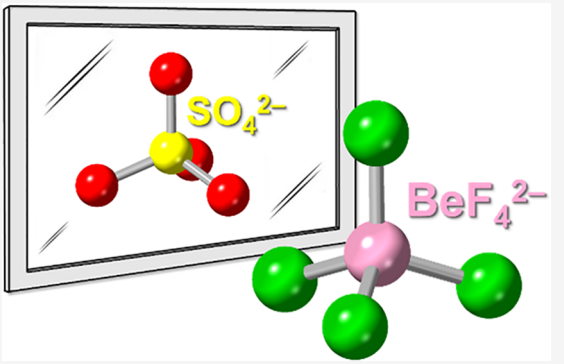

INTRODUCTION

Despite their high toxicity and carcinogenicity, beryllium (Be) and its alloys/compounds are important materials in applications ranging from nonsparking tools to key components for the nuclear and aerospace industries due to a unique combination of physicochemical and mechanical properties.[1] In the presence of fluoride, Be is readily converted to the water-soluble and stable tetrafluoroberyllate anion (BeF_4^{2-}).[2] Tetrafluoroberyllates themselves serve as critical constituents in industrial processes, such as coolants and solvents in nuclear reactors,[3,4] and as intermediates in the production of Be metal.[5]

The chronic Be disease (berylliosis) caused by exposure to Be dust of early workers unaware of the health hazards of Be created a nasty reputation for this otherwise fascinating element, which continues to hinder studies of Be chemistry.[6] For instance, there are only 634 crystal structures containing Be in the Cambridge Structural Database (CSD) to date compared to 6121, 12883, and 81531 structures containing its neighbors in the periodic table, Mg, Li, and B.[7] Furthermore, the supramolecular binding of the BeF_4^{2-} anion has just recently been reported.[8]

BeF_4^{2-} is similar to the sulfate (SO_4^{2-}) anion in that they have identical molecular charge, shape, number of atoms, and number of valence electrons, and they are also similar in size (average Be−F and S−O distances in crystal structures containing noncoordinated BeF_4^{2-} and SO_4^{2-} ions are 1.55(1) and 1.48(1) Å, respectively) (Figure 1).[7] The isomorphism of BeF_4^{2-} and SO_4^{2-} salts was recognized 110 years ago,[9] when it was found that $(NH_4)_2BeF_4$, $(NH_4)_2SO_4$, K_2BeF_4, and K_2SO_4 have very similar molecular volumes and form mixed crystals in all proportions.[10,11] Subsequently, numerous inorganic and organic salts of BeF_4^{2-} isomorphous with analogues containing tetrahedral oxoanions (XO_4^{n-}: n = 2, X = S, Se, Cr, Mo, W, HP; n = 3, X = P, As, V; n = 4, X = Si), including double salts such as alums ($M_2^IAl_2(BeF_4)_4(H_2O)_{24}$), Tutton's salts ($M_2^IM^{II}(BeF_4)_2(H_2O)_6$), and Langbeinites ($M_2^IM_2^{II}(BeF_4)_3$), have been characterized (M = metal, ammonium or organic cation).[2,12,13]

While the isomorphism of BeF_4^{2-} and SO_4^{2-} in salts has been thoroughly studied and is now well established, a corresponding isomorphism of noncovalently bound BeF_4^{2-} in host−guest complexes has been hitherto uncharted. We have recently reported the first examples of supramolecular complexes that bind the BeF_4^{2-} ion exclusively by hydrogen bonds.[8] These complexes are based on nanojar hosts, which

Received: November 1, 2022
Revised: January 17, 2023
Published: January 30, 2023

ACS Publications

© 2023 American Chemical Society

https://doi.org/10.1021/acs.cgd.2c01261
Cryst. Growth Des. 2023, 23, 1676−1688

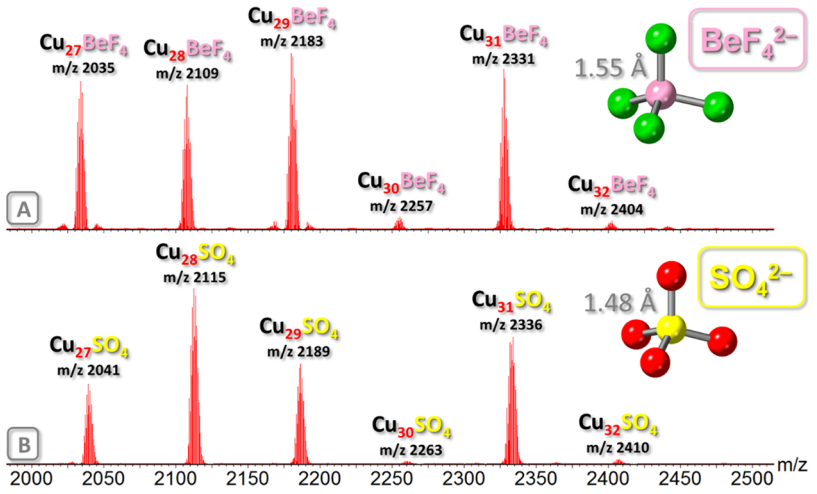

Figure 1. ESI-MS(−) spectra of the as-synthesized (A) tetrafluoroberyllate-nanojar mixture $[BeF_4\subset\{Cu(OH)(pz)\}_n]^{2-}$ (Cu_nBeF_4; n = 27−32) and (B) sulfate-nanojar mixture $[SO_4\subset\{Cu(OH)(pz)\}_n]^{2-}$ (Cu_nSO_4; n = 27−32) in CH_3CN.

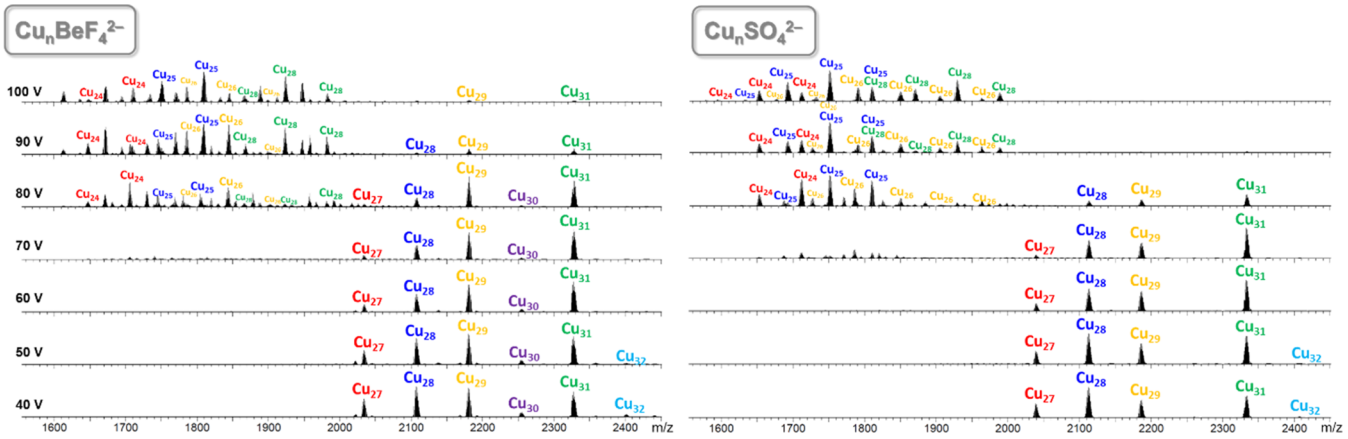

Figure 2. ESI-MS(−) spectra of Cu_nBeF_4 and Cu_nSO_4 (n = 27−32) in CH_3CN at variable sampling cone voltages. Daughter species carry the same color coding as the corresponding parent nanojars.

form a series of oligomerization isomers of the formula $[BeF_4\subset\{cis\text{-}Cu^{II}(\mu\text{-}OH)(\mu\text{-}pz)\}_n]^{2-}$ (Cu_nBeF_4; n = 27−32). Each nanojar consists of three $[cis\text{-}Cu^{II}(\mu\text{-}OH)(\mu\text{-}pz)]_x$ (x = 6−14, except 11) metallamacrocycles, which are bound together by multiple H-bonds and axial Cu···O interactions. Although similar complexes containing an incarcerated SO_4^{2-} anion have been previously prepared and studied,[14−17] details of the supramolecular binding of sulfate by H-bonding in nanojars have only been available so far for an analogue with tethered pz ligands, $[SO_4\subset\{cis\text{-}Cu_{28}(\mu\text{-}OH)_{28}(\mu\text{-}pzCH_2CH_2pz)_{14}\}]^{2-}$.[18,19] Herein, we describe the isomorphism of the $Cu_{28}BeF_4$ and $Cu_{31}BeF_4$ nanojars with the corresponding $Cu_{28}SO_4$ and $Cu_{31}SO_4$ analogues and contrast it with significant differences in bonding within the two anions, leading to the selectivity of nanojars for sulfate. Also, pseudopolymorphism in Cu_nBeF_4 (n = 28, 31, and 32) and $Cu_{31}SO_4$ nanojars will be discussed based on novel single-crystal X-ray structures of $(Bu_4N)_2[BeF_4\subset\{Cu(OH)(pz)\}_{6+12+10}]$ ($Cu_{28}BeF_4$, **1a** (nitrobenzene/pentane) and **1b** (chlorobenzene/pentane)), $(Bu_4N)_2[BeF_4\subset\{Cu(OH)(pz)\}_{8+14+9}]$ ($Cu_{31}BeF_4$, **3a** (toluene) and **3b** (bromobenzene/hexane)), $(Bu_4N)_2[SO_4\subset\{Cu(OH)(pz)\}_{8+14+9}]$ ($Cu_{31}SO_4$, **4a** (chlorobenzene/pentane) and **4b** (1,2-dichlorobenzene/heptane)) and $(Bu_4N)_2[BeF_4\subset\{Cu(OH)(pz)\}_{9+14+9}]$ ($Cu_{32}BeF_4$, **5a** (1,2-dichlorobenzene/heptane)), as well as previously published structures of $(Bu_4N)_2[BeF_4\subset\{Cu(OH)(pz)\}_{6+12+10}]$ ($Cu_{28}BeF_4$, **1c** (toluene)),[8] $(Bu_4N)_2[SO_4\subset\{Cu(OH)(pz)\}_{6+12+10}]$ ($Cu_{28}SO_4$, **2** (toluene)),[15] $(Bu_4N)_2[BeF_4\subset\{Cu(OH)(pz)\}_{8+14+9}]$ ($Cu_{31}BeF_4$, **3c** (chlorobenzene/heptane)),[8] and $(Bu_4N)_2[BeF_4\subset\{Cu(OH)(pz)\}_{9+14+9}]$ ($Cu_{32}BeF_4$, **5b** (1,2-dichlorobenzene/pentane)).[8]

RESULTS AND DISCUSSION

Synthesis and Mass Spectrometric Characterization. Tetrafluoroberyllate- and sulfate-incarcerating nanojars of the formula $(Bu_4N)_2[anion\subset\{cis\text{-}Cu^{II}(\mu\text{-}OH)(\mu\text{-}pz)\}_n]$ (Cu_n, n = 27−32; anion = BeF_4^{2-} or SO_4^{2-}) were obtained from the reaction of $Cu(NO_3)_2{\cdot}2.5H_2O$, pyrazole, Bu_4NOH, and the tetrabutylammonium salt of the anion in tetrahydrofuran (THF). ESI-MS(−) analysis at a sampling cone voltage of 40 V reveals the presence of nanojars with n = 27 ($Cu_{27}BeF_4$, m/z 2035; $Cu_{27}SO_4$, m/z 2041), n = 28 ($Cu_{28}BeF_4$, m/z 2109; $Cu_{28}SO_4$, m/z 2115), n = 29 ($Cu_{29}BeF_4$, m/z 2183; $Cu_{29}SO_4$, m/z 2189) and n = 31 ($Cu_{31}BeF_4$, m/z 2331; $Cu_{31}SO_4$, m/z 2336), along with small amounts of nanojars with n = 30 ($Cu_{30}BeF_4$, m/z 2257; $Cu_{30}SO_4$, m/z 2263) and n = 32 ($Cu_{32}BeF_4$, m/z 2404; $Cu_{32}SO_4$, m/z 2410) (Figure 1).

https://doi.org/10.1021/acs.cgd.2c01261
Cryst. Growth Des. 2023, 23, 1676−1688

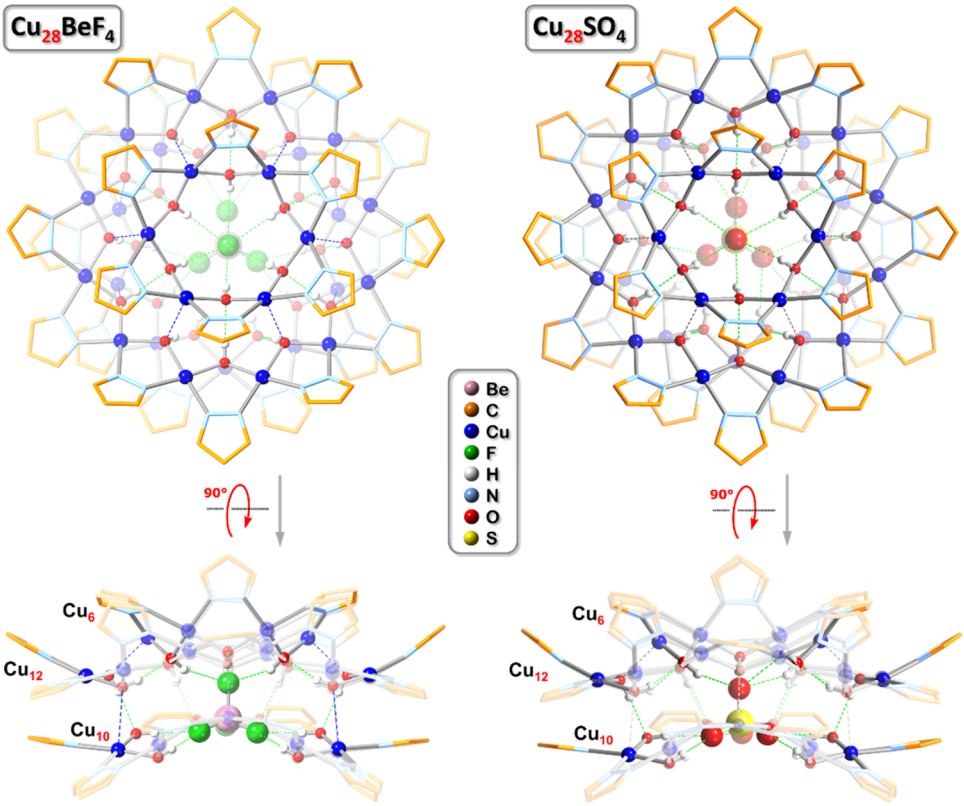

Figure 3. Comparison of the isomorphous crystal structures of $Cu_{28}BeF_4$ (**1c**) and $Cu_{28}SO_4$ (**2**) (top and side views). Green and blue dotted lines indicate hydrogen bonds and axial Cu···O interactions, respectively. Counterions, lattice solvent molecules, and C−H bond H-atoms are omitted for clarity, and only the major component is shown for disordered moieties.

Table 1. Structural Parameters of Noncoordinated BeF_4^{2-} and SO_4^{2-} Ions (based on the CSD)[7] along with H-Bonding Data in the Corresponding Nanojars (with D···A Distances up to 3.2 Å)

anion	average Be−F or S−O (Å)	average F···F or O···O within anion (Å)	donor/acceptorO···F/O range for H-bonds to anion (Å)	average O···F/O distance for H-bonds to anion (Å)
BeF_4^{2-}	1.548(2)	2.526(2)	2.66(1)−3.18(2) ($Cu_{6+12+10}$)	2.89(2)
			2.72(2)−3.20(2) (Cu_{8+14+9})	2.94(2)
			2.59(3)−3.18(1) (Cu_{9+14+9})	2.93(3)
SO_4^{2-}	1.473(3)	2.399(3)	2.73(2)−3.19(2) ($Cu_{6+12+10}$)	2.92(1)
			2.79(1)−3.20(1) (Cu_{8+14+9})	2.98(1)

The behavior of the Cu_nBeF_4 and Cu_nSO_4 nanojars at different ESI-MS(−) sampling cone voltages has also been studied. The signal intensities of both Cu_nBeF_4 and Cu_nSO_4 nanojars increase from 0 to 40 V. Above 40 V, the nanojar signal intensities begin to decrease, and the peaks in the m/z 2030−2410 window gradually disappear, while increasing amounts of daughter nanojar peaks appear in the m/z 1550−2030 window (Figure 2). At 100 V, no parent nanojars, but only daughter species are detected, along with $[Cu(pz)_2]^-$ at m/z 198. In ESI-MS(+), only the counterion (Bu_4N^+) is observed at m/z 242. The daughter species correspond to shrunken $[Cu_{n-3}O_{(n-y+2)/2}(pz)_{n+y-8}(anion)]^{2-}$ nanojars, which form by losing a $Cu_3(OH)_6(Hpz)_{8-y}(H_2O)_{(n+y-14)/2}$ fragment ($y = (-1) - 8$) from the parent nanojars. Cu_nBeF_4 nanojars appear to be more resilient than Cu_nSO_4, as small amounts persist even at 100 V. In the case of Cu_nBeF_4, additional hitherto unidentified peaks are also observed.

X-ray Crystallography. From the as-synthesized Cu_nSO_4 nanojar mixture, individual crystals of most components found in significant amounts (n = 28, $Cu_{6+12+10}SO_4$; n = 29, $Cu_{8+13+8}SO_4$; n = 31, $Cu_{8+14+9}SO_4$) were grown,[15,17] except for n = 27 ($Cu_{6+12+9}SO_4$) and n = 29 ($Cu_{7+13+9}SO_4$). From the corresponding Cu_nBeF_4 nanojar mixture, X-ray diffraction quality crystals could only be obtained so far for n = 28 ($Cu_{6+12+10}BeF_4$), n = 31 ($Cu_{8+14+9}BeF_4$), and n = 32 ($Cu_{9+14+9}BeF_4$).[8] Despite being a very minor component in the nanojar mixture, $Cu_{32}BeF_4$ formed good-quality single crystals, whereas $Cu_{27}BeF_4$ and $Cu_{29}BeF_4$ did not. In an attempt to grow crystals of the missing nanojars for analysis of their structure and anion binding details, numerous crystal growing setups based on different solvent combinations, counterions, and additives were employed. Thus far, these efforts resulted in new pseudopolymorphs of $Cu_{28}BeF_4$ (**1a** and **1b**), $Cu_{31}BeF_4$ (**3a** and **3b**), $Cu_{32}BeF_4$ (**5a**), and $Cu_{31}SO_4$ (**4a** and **4b**). The latter provide good quality H-bonding data, which was not available earlier for the $Cu_{31}SO_4$ structure crystallized from toluene/hexanes.[15]

Nanojar structures **1b**, **1c** ($Cu_{28}BeF_4$), and **2** ($Cu_{28}SO_4$) are isomorphous (triclinic, $P\bar{1}$; Table S1). In addition, **1a** (also triclinic $P\bar{1}$, with a different unit cell) is a pseudopolymorph of **1b** and **1c** with nitrobenzene/pentane solvent molecules included in the crystal lattice compared to chlorobenzene/

https://doi.org/10.1021/acs.cgd.2c01261
Cryst. Growth Des. 2023, 23, 1676−1688

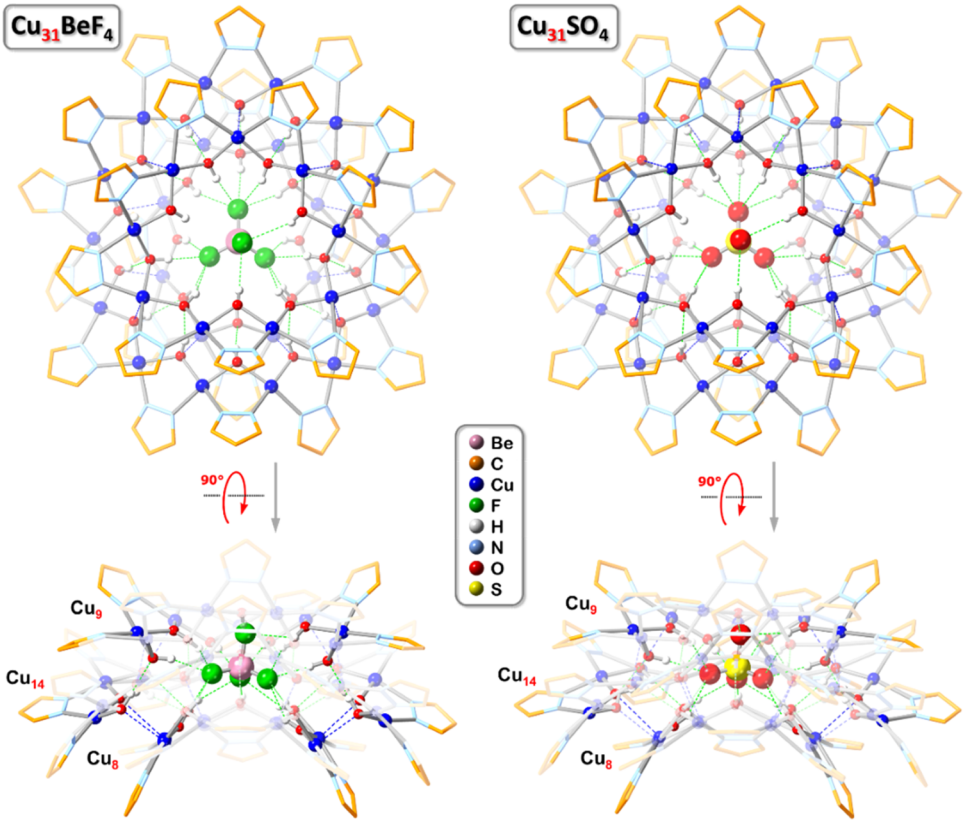

Figure 4. Comparison of the isomorphous crystal structures of $Cu_{31}BeF_4$ (**3c**) and $Cu_{31}SO_4$ (**4a**) (top and side views). Green and blue dotted lines indicate hydrogen bonds and axial Cu···O interactions, respectively. Counterions, lattice solvent molecules, and C−H bond H-atoms are omitted for clarity, and only the major component is shown for disordered moieties.

pentane (**1b**) and toluene (**1c**, **2**). The crystal structures of $Cu_{28}BeF_4$ (**1c**) and the analogous $Cu_{28}SO_4$ (**2**) are shown in Figure 3, while the structures of the different $Cu_{28}BeF_4$ polymorphs (**1a**−**c**) are contrasted in Figure S1. A detailed analysis reveals only minor differences within the Cu_n-rings of **1a**−**c** and **2**, with consistent average Cu−O bond lengths of 1.928(3)−1.931(3) Å, average Cu−N bond lengths of 1.971(4)−1.980(4) Å, average N−Cu−O (*trans*) angles of 172.1(1)−172.5(1)°, average N−Cu−O (*cis*) angles of 85.6(2)−85.8(1)°, and average Cu···Cu distances of 3.277(1)−3.286(1) Å, respectively (Tables S4 and S9−S11). The noncovalent interactions between individual Cu_n-rings are also quite similar, with average axial Cu···O distances of 2.481(3)−2.516(3) Å, and average H-bonded O···O distances of 2.764(6)−2.778(3) Å (Tables S4 and S18−S20). In terms of H-bonding parameters between Cu_n-rings and the incarcerated BeF_4^{2-} or SO_4^{2-} anion, an average O···F distance of 2.89(1) Å is observed in **1** compared to the average O···O distance of 2.92(1) Å in **2** (Tables 1 and S4).

Nanojar structures **3b**, **3c** ($Cu_{31}BeF_4$), and **4a** ($Cu_{31}SO_4$) are also isomorphous (Table S2). **3a** is a pseudopolymorph (toluene) of **3b** (bromobenzene) and **3c** (chlorobenzene), whereas **4b** (1,2-dichlorobenzene) is a pseudopolymorph of **4a** (chlorobenzene). All Cu_{31} nanojars have the same triclinic $P\bar{1}$ symmetry. Figures 4 and S2 show that the structures of analogous $Cu_{31}BeF_4$ (**3c**) and $Cu_{31}SO_4$ (**4a**) nanojars, as well as their respective polymorphs **3a**, **3b**, and **4b**, are again very similar, with average Cu−O and Cu−N bond lengths of 1.923(3)−1.928(6) and 1.970(4)−1.975(8) Å, average N−Cu−O (*trans*) and N−Cu−O (*cis*) angles of 171.4(2)−172.4(3)° and 85.7(2)−86.1(2)°, and average Cu···Cu distances of 3.286(1)−3.293(2) Å within their Cu_n-rings (Tables S5 and S12−S16). The noncovalent interactions between individual Cu_n-rings have slightly larger values for the corresponding interatomic distances than in the Cu_{28} nanojars, with average axial Cu···O distances of 2.515(5)−2.551(1) Å and average H-bonded O···O distances of 2.834(7)−2.869(5) Å (Tables S5 and S21−S25). The average H-bonded O···F distances between Cu_n-rings and BeF_4^{2-} ions range from 2.92(3) to 2.95(3) Å, whereas the corresponding O···O distances between Cu_n-rings and SO_4^{2-} ions range from 2.95(3) to 3.00(1) Å (Tables 1 and S5).

The two pseudopolymorphs of $Cu_{32}BeF_4$ (**5a** with 1,2-dichlorobenzene/heptane and **5b** with 1,2-dichlorobenzene/pentane) display a much higher crystallographic symmetry (orthorhombic, $P2_12_12_1$) than the Cu_{28} and Cu_{31} nanojars (triclinic, $P\bar{1}$) (Table S3). Nevertheless, they also contain an entire nanojar moiety in the asymmetric unit, located on a general position (Figure 5). The average Cu−O and Cu−N bond lengths of 1.933(4)/1.932(4) and 1.976(5)/1.976(5) Å, average N−Cu−O *trans* and *cis* angles of 172.4(2)/172.6(2)° and 85.9(2)/85.8(2)°, and average Cu···Cu distances of 3.279(1)/3.278(1) Å within the Cu_n-rings of **5a** and **5b**, respectively, are practically identical (Tables S6 and S17). So are the average axial Cu···O distances of 2.525(4)/2.530(4) Å and the average H-bonded O···O distances of 2.797(6)/2.800(5) Å between individual Cu_n-rings, as well as the average H-bonded O···F distances of 2.94(3) Å and 2.91(3) Å between Cu_n-rings and the incarcerated BeF_4^{2-} anion (Tables 1, S6 and S26).

https://doi.org/10.1021/acs.cgd.2c01261
Cryst. Growth Des. 2023, 23, 1676−1688

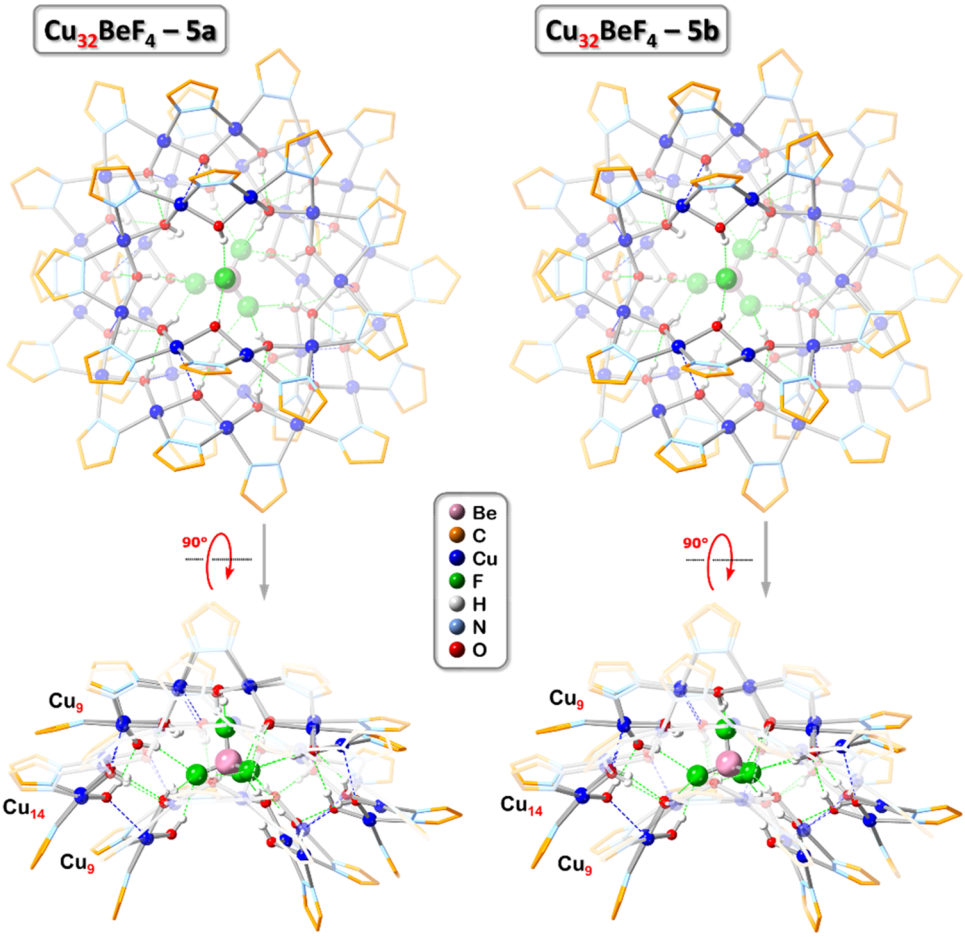

Figure 5. Comparison of the crystal structures of the two pseudopolymorphs of $Cu_{32}BeF_4$ (**5a** and **5b**) (top and side views). Green and blue dotted lines indicate hydrogen bonds and axial Cu···O interactions, respectively. Counterions, lattice solvent molecules, and C−H bond H-atoms are omitted for clarity, and only the major component is shown for disordered moieties.

All Cu centers of the larger central rings (Cu_{12} or Cu_{14}) in all nanojars studied are four-coordinate in a slightly distorted square-planar *cis*-CuN_2O_2 coordination environment. In contrast, the Cu centers of the Cu_6 side-rings in the Cu_{28} nanojars are all square-pyramidal, having an additional O atom in the axial position with Cu···O distances ranging from 2.338(2) to 2.456(3) Å (the sum of the van der Waals radii of Cu and O is 2.92 Å). In the Cu_8 side-rings of the Cu_{31} nanojars, all Cu centers are also square-pyramidal with Cu···O distances ranging from 2.338(3) to 2.899(3) Å (except in **4b**, in which only seven Cu centers have axial Cu···O distances shorter than 2.92 Å). In the Cu_9 side-rings, only five Cu centers are square-pyramidal (axial Cu···O: 2.332(3)−2.817(4) Å) in the Cu_{31} nanojars (except for **4b**, in which one nanojar unit has six and the second unit has seven axial Cu···O distances shorter than 2.92 Å) and only seven are square-pyramidal in the Cu_{32} nanojars (axial Cu···O: 2.347(4)−2.888(4) Å). Only four (or six in **1a**) of the Cu centers of the Cu_{10} side-rings are square-pyramidal in the Cu_{28} nanojars (axial Cu···O: 2.345(2)−2.898(2) Å).

To further investigate the slight structural differences observed in the eleven nanojar structures discussed here, the orientations of the pyrazolate moieties relative to the adjacent Cu−O−Cu units were analyzed (Tables S7 and S8). Specifically, the dihedral angles were measured between the mean planes defined by the five atoms of the pyrazolate ring and the three atoms of the Cu−O−Cu unit, along with the component fold- and twist angles (Figure 6). The average fold angles in the larger, flatter central rings (Cu_{12} or Cu_{14}) vary between 36.4(6)−47.9(7)° in the 11 different structures, whereas the values for the two smaller, more puckered side rings vary between 50.7(2)−55.1(4)° (Cu_9 or Cu_{10}) and 44.1(3)−52.7(2)° (Cu_6, Cu_8 or Cu_9). The corresponding average twist angles vary between 4.3(2)−6.6(2)° in the central rings (Cu_{12} or Cu_{14}) and between 2.1(2)−4.6(3)° (Cu_9 or Cu_{10}) and 1.7(1)−5.8(2)° (Cu_6, Cu_8 or Cu_9) in the two side-rings. Thus, only a small variation of <12° is observed for the fold angle averages and an even smaller variation of <5° for the twist angle averages, although the individual fold angles (0.7(6)−80.2(3)°) and twist angles (0.02(9)−21.7(4)°) vary more broadly by 80 and 22°, respectively.

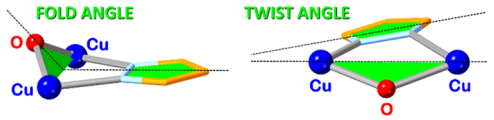

Figure 6. Illustration of the fold and twist angles contributing to the dihedral angles observed in nanojars **1**−**5**.

To illustrate the flexibility of the $[Cu(OH)(pz)]_x$ rings in the nanojars, the structures of the $[Cu(OH)(pz)]_9$ rings in different nanojars were compared. Figure 7 shows not only that

https://doi.org/10.1021/acs.cgd.2c01261
Cryst. Growth Des. 2023, 23, 1676−1688

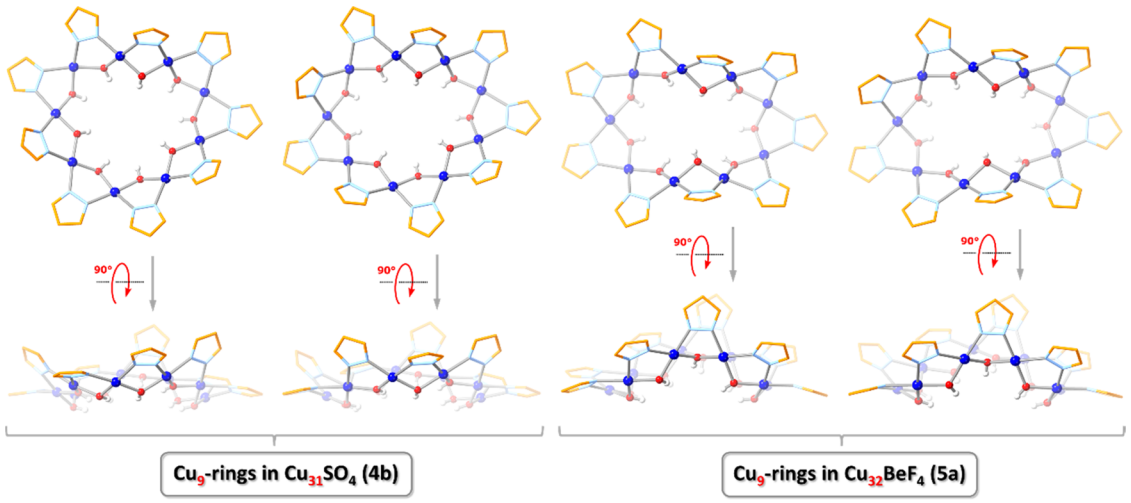

Figure 7. Comparison of the structures of the Cu_9-rings in the two crystallographyically independent nanojar units of $Cu_{8+14+9}SO_4$ (**4b**) and in $Cu_{9+14+9}BeF_4$ (**5a**) (top and side views). No disorder is observed in any of these four Cu_9 rings.

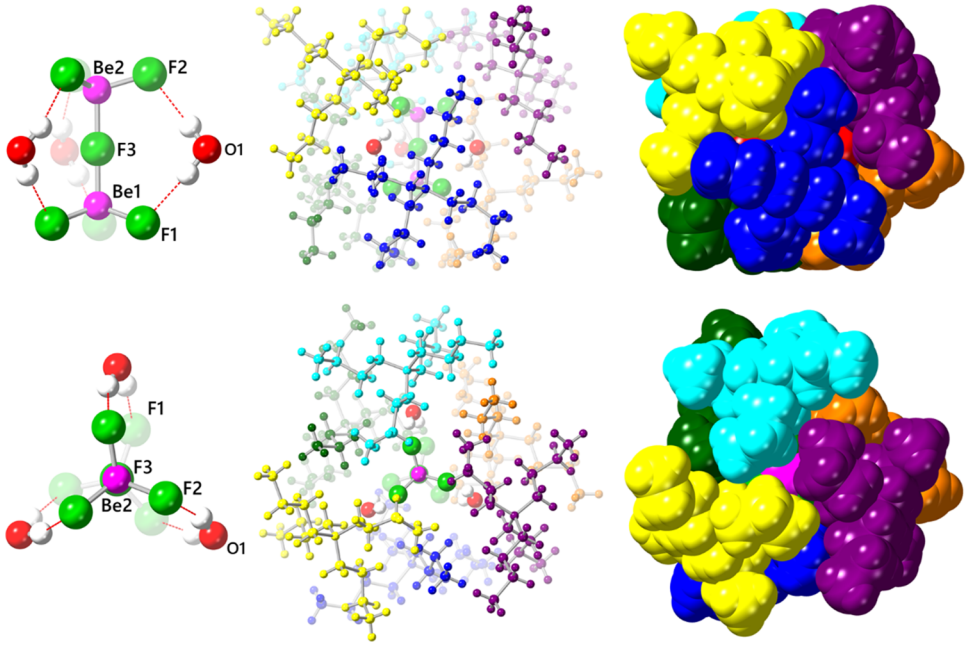

Figure 8. Side views (upper row) and top views (along a C_3-axis, lower row) of the crystal structure of $(Bu_4N)_3Be_2F_7(H_2O)_3$. The six different Bu_4N^+ cations surrounding the $Be_2F_7^{2-}$ anion are highlighted in different colors.

the Cu_9 rings are significantly more folded in $Cu_{32}BeF_4$ (**5a**) than in $Cu_{31}SO_4$ (**4b**) but also that they differ in shape even within the same structure ($Cu_{9+14+9}BeF_4$ contains two different Cu_9 rings, and there are two crystallographically independent $Cu_{8+14+9}SO_4$ nanojar units in **4b**).

Attempts to grow crystals of the simple tetrabutylammonium salt of tetrafluoroberyllate, $(Bu_4N)_2BeF_4$, have not been successful so far, likely due to its highly hygroscopic nature. Instead, we obtained crystals of $(Bu_4N)_3Be_2F_7(H_2O)_3$ from a nitrobenzene/toluene solution of $(Bu_4N)_2BeF_4$ by pentane vapor diffusion (Table S3). In this high symmetry lattice (cubic $Pa\bar{3}$, same as of FeS_2), a twisted (by 27.4(3)°) trigonal prismatic $Be_2F_7^{3-}$ anion (Be1−F1: 1.543(2), Be1−F3 1.576, Be2−F2 1.530(3), Be2−F3 1.642(7) Å) is located on a C_3-axis inside a capsule formed by six different Bu_4N^+ cations (Figure 8). Each edge of the twisted trigonal prism (F1···F2: 4.189(3) Å) is capped by a water molecule (O−H: 0.875(19) Å; H−O−H: 107(4)°), which bridges the F atoms by H-bonding (O···F distances: 2.713(3) and 2.696 (3) Å, H···F distances: 1.85(2) and 1.85(2) Å, O−H···F angles: 170(5) and 162(5)° to F1 and F2, respectively).

Only one other crystal structure containing the $Be_2F_7^{3-}$ anion exists in the CSD.[20] In this anhydrous structure (space group: $Ia\bar{3}$), the $Be_2F_7^{3-}$ anion has a staggered conformation (symmetry point group: D_{3d}) instead of the gauche conformation (symmetry point group: D_3) observed in $(Bu_4N)_3Be_2F_7(H_2O)_3$. Two crystal structures containing the $Be_2F_6^{2-}$ anion (in which two F atoms bridge the two Be centers) are also found in the CSD,[21,22] as well as one containing a polymeric $(BeF_3^-)_n$ chain.[23]

The $Be_2F_7^{3-}$ anion is structurally analogous to $S_2O_7^{2-}$ (disulfate or pyrosulfate). In $S_2O_7^{2-}$, however, the S−O−S angle is 121−128° compared to the ∼180° observed for Be−F−Be in the two crystal structures of $Be_2F_7^{3-}$. To obtain

https://doi.org/10.1021/acs.cgd.2c01261
Cryst. Growth Des. 2023, 23, 1676−1688

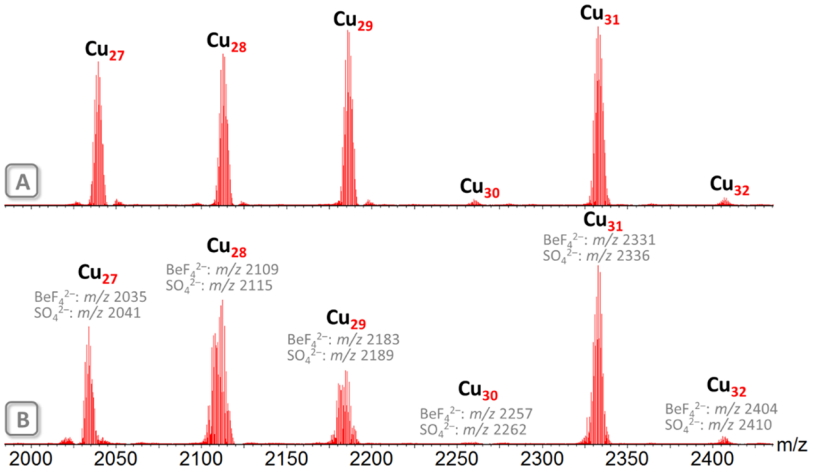

Figure 9. ESI-MS(−) spectra in CH_3CN of (A) the as-synthesized nanojar mixture obtained using a 1:1 molar mixture of BeF_4^{2-} and SO_4^{2-} ions, and (B) a 1:1 molar mixture of presynthesized $[BeF_4⊂\{Cu(OH)(pz)\}_n]^{2-}$ and $[SO_4⊂\{Cu(OH)(pz)\}_n]^{2-}$ (n = 27−32).

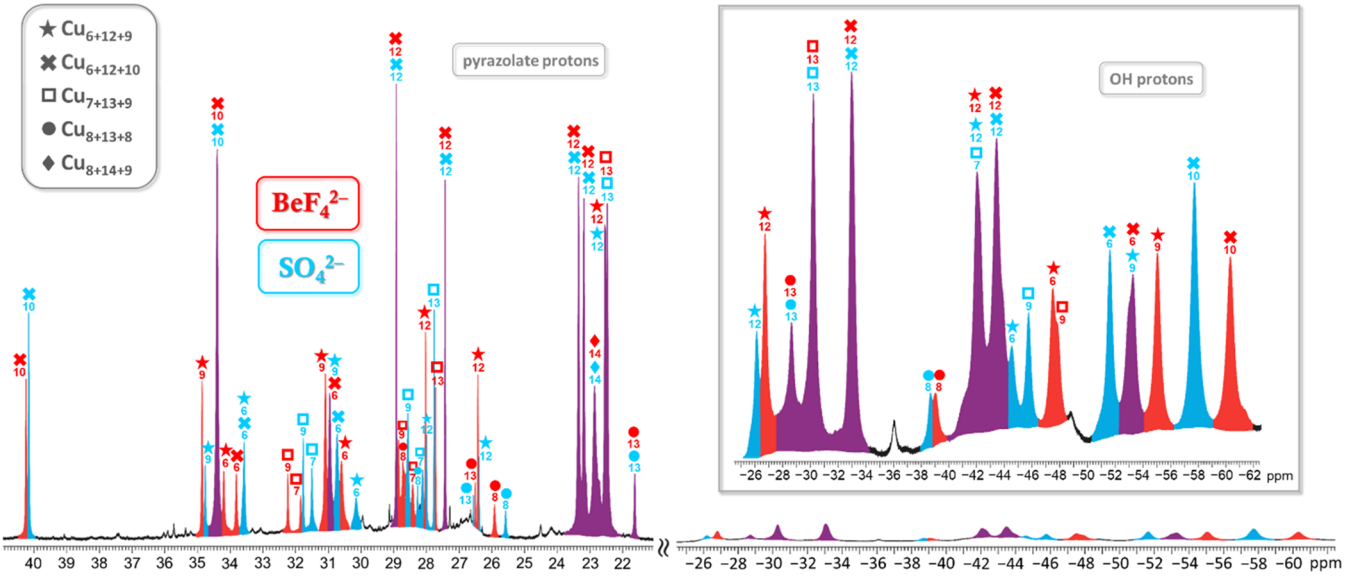

Figure 10. Comparison of the ^{1}H NMR spectra in DMSO-d_6 of BeF_4- (red) and SO_4-nanojars (blue) recorded on a solution containing a 1:1 molar mixture of presynthesized Cu_nBeF_4 and Cu_nSO_4 (n = 27−31). Purple indicates overlapping red and blue peaks.

$S_2O_7^{2-}$ from HSO_4^-, heating to ∼200 °C is needed ($2HSO_4^- \rightarrow S_2O_7^{2-} + H_2O$).[24] In contrast, $Be_2F_7^{3-}$ forms from BeF_4^{2-} at room temperature ($2BeF_4^{2-} \rightarrow Be_2F_7^{3-} + F^-$). $S_2O_7^{2-}$ easily hydrolyzes back to HSO_4^- in aqueous solution,[25] whereas $Be_2F_7^{3-}$ appears to be stable.

Selectivity of Nanojars for Sulfate vs Tetrafluoroberyllate. Given the pronounced structural similarity between the BeF_4^{2-} and SO_4^{2-} ions and the observed isomorphism between the corresponding tetrafluoroberyllate- and sulfate-incarcerating nanojars, no distinct selectivity of the nanojars for either anion was initially expected. A selectivity experiment was carried out using a 1:1 molar mixture of BeF_4^{2-} and SO_4^{2-} ions by stirring $(Bu_4N)_2BeF_4$ and $(Bu_4N)_2SO_4$ with $Cu(NO_3)_2$, pyrazole, and Bu_4NOH in THF and isolating the resulting nanojar mixture by precipitation with water. ESI-MS(−) of the product shows the formation of Cu_n (n = 27−32) nanojars. However, the close molecular weight of a given nanojar with either BeF_4^{2-} or SO_4^{2-} hinders the assessment of the ratio between the two anions (Figure 9A). Indeed, the m/z difference between BeF_4- and SO_4-nanojars is only 5.5 units, whereas the isotopic envelope of each nanojar extends over 10 m/z units. Figure 9B shows the mass spectrum obtained for a 1:1 molar mixture of presynthesized Cu_nBeF_4 and Cu_nSO_4 (n = 27−32) nanojars, documenting the overlapping of the corresponding peaks.

While the relative ratio between BeF_4- and SO_4-nanojars cannot be unambiguously established by mass spectrometry, ^{1}H NMR spectroscopy reveals a strong preference of nanojars for SO_4^{2-} over BeF_4^{2-}. First, the ^{1}H NMR signatures of Cu_nBeF_4 and Cu_nSO_4 nanojars were compared. As seen in Figure 10, several nanojar protons show clearly distinguishable peaks with BeF_4^{2-} compared to SO_4^{2-}. Although many of these pairs of peaks are too close to each other or overlap with neighboring peaks, preventing accurate integration, the peaks corresponding to pz-3,5 protons of the Cu_8-ring of the Cu_{8+13+8} nanojars are distinct enough (BeF_4^{2-}: 25.91 ppm; SO_4^{2-}: 25.57 ppm) to provide an estimate of the selectivity. The identity of these peaks was confirmed earlier on samples of pure BeF_4- or SO_4-nanojars.[8,17] Thus, integration of these two peaks in the spectrum obtained for the product of the selectivity experiment

https://doi.org/10.1021/acs.cgd.2c01261
Cryst. Growth Des. 2023, 23, 1676−1688

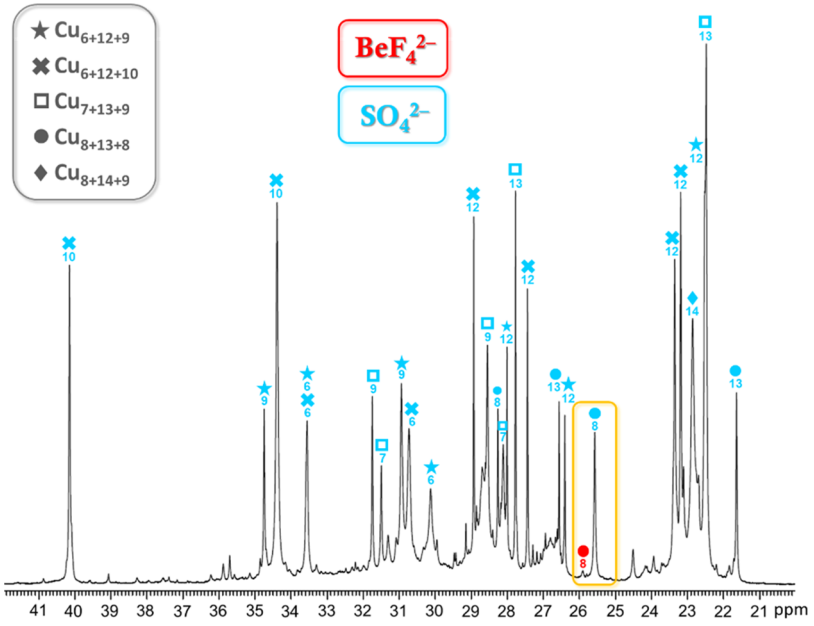

Figure 11. ^{1}H NMR spectrum in DMSO-d_6 of the as-synthesized nanojar mixture prepared using a 1:1 molar mixture of BeF_4^{2-} and SO_4^{2-} ions. The highlighted area between 25 and 26 ppm shows the peaks used for the assessment of selectivity of nanojars for SO_4^{2-} (blue) vs BeF_4^{2-} (red).

using a 1:1 molar mixture of tetrafluoroberyllate and sulfate ions indicates a BeF_4^{2-}/SO_4^{2-} ratio of approximately 1:30 (Figure 11).

To understand the strong preference of nanojars for SO_4^{2-} over BeF_4^{2-}, the binding of these two ions by H-bonding was examined. The binding of sulfate by H-bonds has been documented in various supramolecular hosts,[26,27] whereas nanojars are the first reported hosts that bind the BeF_4^{2-} anion by H-bonds.[8] Previous infrared spectroscopic studies on the BeF_4^{2-} ion as hydrogen-bond acceptor were performed by comparing the spectroscopic features of pairs of isomorphous salts: $[Cu(NH_3)_4]X{\cdot}H_2O$, $[Cu(bipy)]X{\cdot}2H_2O$ and $(NH_4)_2NiX_2{\cdot}H_2O$ (X = BeF_4^{2-} or SO_4^{2-}).[28] Contrary to the intuitive assumption that the interactions involving the more electronegative F atoms as H-bond acceptors should be stronger than those in which O atoms play the role of H-bond acceptors, the IR spectroscopic studies (and related quantum chemical considerations)[29] do not support BeF_4^{2-} as a better H-bond acceptor than SO_4^{2-}.

Because it has a small size and high charge, beryllium has a greater tendency to form covalent bonds than other alkaline-earth metal ions and shows a diagonal relationship with aluminum. Nevertheless, the Pauling electronegativity difference between Be (1.57) and F (3.98) is 2.41, much larger than the corresponding difference of 0.86 between S (2.58) and O (3.44). Furthermore, computational studies of electron density distribution have shown that the atomic charges on Be and F in BeF_4^{2-} are +1.8 and −0.95, close to the values of +2 and −1 in a fully ionic model.[30] In contrast, the atomic charges of +2.4 and −1.1 on S and O in SO_4^{2-} are very different from the values of a fully ionic model (+6 and −2).[31,32] These results point to a largely ionic character for BeF_4^{2-}, whereas SO_4^{2-} is a mostly covalent species. The ionic character of BeF_4^{2-} is evidenced in practice by the fact that while the ion is stable at 650 °C (in molten Na_2BeF_4)[33] as well as in the gas phase,[34,35] it partially forms $[BeF_3(H_2O)]^-$ in aqueous solution at neutral pH.[36−38] With regard to their H-bonding ability, the larger atomic charge on O in SO_4^{2-} (−1.1) than that on F in BeF_4^{2-} (−0.95) is in agreement with the former ion being a stronger H-bond acceptor than the latter.

CONCLUSIONS

The X-ray crystallographic studies presented here demonstrate that the isomorphism observed earlier for simple salts of the BeF_4^{2-} and SO_4^{2-} anions extends into the supramolecular realm. For the first time, an extensive and detailed analysis of 11 nanojar structures related either by isomorphism (Cu_nBeF_4 vs Cu_nSO_4, n = 28 and 31) or pseudopolymorphism (different solvates of $Cu_{28}BeF_4$, $Cu_{31}BeF_4$, $Cu_{32}BeF_4$, and $Cu_{31}SO_4$) has been carried out. The results reveal that the remarkable flexibility of the various Cu_x rings (in this study, x = 6, 8, 9, 10, 12, and 14), leading to distinctive shapes for the Cu_{28}, Cu_{31}, and Cu_{32} nanojars, is based on subtle differences in the coordination environment of the individual Cu centers. The coordination geometry of Cu varies from square-planar to square-pyramidal, with the axial O atom anywhere between 2.332(3) Å and 2.92 Å (the sum of the van der Waals radii of Cu and O). In terms of bond lengths and angles, Cu−O and Cu−N distances vary by less than 0.1 Å, whereas *cis* and *trans* N−Cu−O angles vary by 21 and 8°, respectively (Tables S4−S6). An even larger variation is observed for the individual fold and twist angles between the mean planes of pz rings and Cu−O−Cu units they are bonded to, which vary by 80 and 22°, respectively. It appears that the very existence of nanojars is enabled by the "coordination acrobat" qualities of the Cu^{2+} ion. Indeed, an earlier study showed that nanojars can only be obtained with Cu^{2+} ions, none of which could be substituted by any of the 16 different metal ions tested.[39] On the whole, the flexibility of the nanojar framework allows for the incarceration of different anions with slightly different dimensions in a nanojar of a given size, resulting in the formation of isomorphous structures in the case of Cu_nBeF_4 and Cu_nSO_4.

Despite their flexibility, nanojars do not pack well in three-dimensional (3D) lattices. This is perhaps due to their toroidal shape, which leaves large voids in the corresponding crystal

https://doi.org/10.1021/acs.cgd.2c01261
Cryst. Growth Des. 2023, 23, 1676−1688

lattices. These voids are only partially filled by the two countercations (Bu_4N^+), with the remainder containing several highly disordered solvent molecules. Regardless of the solvent used for crystallization of the different pseudopolymorphs, the weakness of nanojar lattices is evident from the quick solvent loss upon removal of the crystal from the mother liquor, leading to opacity and ultimately to disintegration of the crystal.

Nanojar selectivity studies for SO_4^{2-} vs BeF_4^{2-} show a pronounced (30-fold) preference for sulfate. Because X-ray crystallographic studies do not indicate significant differences in the H-bonding pattern around the two anions in nanojars of a given size, the observed selectivity is attributed to the larger atomic charge on O in SO_4^{2-} (−1.1) than that on F in BeF_4^{2-} (−0.95). The atomic charges on the central and peripheral atoms also suggest that BeF_4^{2-} is essentially ionic, whereas SO_4^{2-} is covalent. The crystallization of $(Bu_4N)_3Be_2F_7(H_2O)_3$ from a solution of $(Bu_4N)_2BeF_4$, resulting in the formation of the $Be_2F_7^{3-}$ ion, is further testament to the ionic nature of BeF_4^{2-}.

EXPERIMENTAL SECTION

WARNING! Beryllium metal and its compounds are extremely toxic and carcinogenic if inhaled, swallowed, or in contact with skin. Appropriate precautions should be taken while handling and disposing of all beryllium-containing materials.

Synthesis. All commercially available chemicals were used as received. Deionized water was freshly boiled and cooled to room temperature under nitrogen gas. $(Bu_4N)_2BeF_4$,[8] $(Bu_4N)_2[BeF_4⊂\{Cu(OH)(pz)\}_n]$ (Cu_nBeF_4; n = 27−32) and $(Bu_4N)_2[SO_4⊂\{Cu(OH)(pz)\}_n]$ (Cu_nSO_4; n = 27−32) were synthesized according to published procedures.[8,17]

Characterization of the 1:1 Molar Mixture of Tetrafluoroberyllate and Sulfate Nanojars. A mixture of Cu_nBeF_4 (0.0175 g, 3.6×10^{-3} mmol) and Cu_nSO_4 (0.0175 g, 3.6×10^{-3} mmol) was dissolved in DMSO-d_6 (0.6 mL). The solution was filtered, and a few drops were diluted with acetonitrile for mass spectrometric analysis (Figure 9B). The remainder was transferred into an NMR tube for ^{1}H NMR analysis (Figure 10). NMR spectra were collected on a Jeol JNM-ECZS (400 MHz) instrument.

Anion Selectivity of Nanojars for SO_4^{2-} vs BeF_4^{2-}. A 50 mL three-neck round-bottom flask equipped with a pressure-equalizing addition funnel and a stir bar was charged with $Cu(NO_3)_2·2.5H_2O$ (0.5000 g, 2.15 mmol), pyrazole (0.1464 g, 2.15 mmol), $(Bu_4N)_2BeF_4·xH_2O$ (x = 1.93; 1.2833 g, 2.15 mmol), $(Bu_4N)_2SO_4$ (50% in H_2O, 2.4979 g, 2.15 mmol), and 20 mL of THF. The flask was purged with N_2, and Bu_4NOH (1 M in H_2O, 4.30 mL, 4.30 mmol) was added dropwise from the addition funnel to the reaction solution under stirring. The deep-blue solution was cannulated into water (200 mL) under stirring. The blue precipitate was filtered off, washed thoroughly with water, and dried under high vacuum. The resulting dark blue powder (0.2735 g) was analyzed by ESI-MS (Figure 9A) and ^{1}H NMR (Figure 11).

Mass Spectrometry. Mass spectrometric analysis of the nanojars was performed with a Waters Synapt G1 HDMS instrument, using electrospray ionization (ESI). 10^{-4}−10^{-5} M solutions were prepared in CH_3CN. Samples were infused by a syringe pump at 5 μL/min, and nitrogen was supplied as the nebulizing gas at 500 L/h. The electrospray capillary voltage was set to −2.5 or +2.5 kV, respectively, with a desolvation temperature of 110 °C. The sampling and extraction cones were maintained at 40 V (except for the varying sampling cone voltage experiment, 0−100 V) and 4.0 V, respectively, at 80 °C.

X-ray Crystallography. Single crystals were grown at room temperature by n-pentane vapor diffusion into a nitrobenzene/toluene (**1a**) or chlorobenzene (**1b**) solution of Cu_nBeF_4 (n = 27−32), by vapor diffusion of hexanes into a bromobenzene solution of Cu_nBeF_4 (n = 27−32) in the presence of 1-chloro-2,4-dinitrobenzene (**3a**), by slow evaporation of a toluene solution of Cu_nBeF_4 (n = 27−32) (**3b**), by vapor diffusion of n-pentane or n-heptane into a solution of $Cu_{31}SO_4$ in chlorobenzene (**4a**) or 1,2-dichlorobenzene(**4b**), respectively, and by vapor diffusion of n-heptane into a 1,2-dichlorobenzene solution of Cu_nBeF_4 (n = 27−32) in the presence of 1,3,5-trichlorobenzene (**5a**). Crystals of $(Bu_4N)_3Be_2F_7(H_2O)_3$ were obtained from a nitrobenzene/toluene solution of $(Bu_4N)_2BeF_4·xH_2O$ ($x \approx 1.93$) by pentane vapor diffusion. Once removed from the mother liquor, nanojar crystals were very sensitive to solvent loss at ambient conditions and were mounted quickly under a cryostream (150 K) to prevent decomposition. X-ray diffraction data were collected from a single crystal mounted atop a MiTeGen micromesh mount under Fomblin oil with a Bruker AXS D8 Quest diffractometer equipped with a Photon II charge-integrating and photon counting pixel array detector (CPAD) using a fine focus sealed X-ray tube with graphite-monochromated Mo-K_α (λ = 0.71073 Å) radiation (for **1a**, **3a** and **4b**) or a Bruker AXS D8 Quest diffractometer with Photon III C14 CPAD using a microfocus X-ray tube with multilayer optics for monochromatization with Cu-K_α (λ = 1.54178 Å) radiation (for **1b**, **3b**, **4a**, **5a** and $(Bu_4N)_3Be_2F_7(H_2O)_3$). The data were collected using APEX3 or APEX4,[40] integrated using SAINT,[41] and scaled and corrected for absorption and other effects using SADABS.[42] The structures were solved by employing direct or dual methods using ShelXS[43] or ShelXT[44] and refined by full-matrix least-squares on F^2 using ShelXL.[45] C−H hydrogen atoms were placed in idealized positions and refined using the riding model. Thermal ellipsoid plots are provided in the SI (Figures S3−S10).

1a. Hydroxyl H atom positions were refined, and O−H distances were restrained to a target value of 0.84(2) Å. The BeF_4^{2-} anion was refined as twofold disordered. The two moieties were restrained to have similar geometries. U_{ij} components of ADPs for disordered atoms closer to each other than 2.0 Å were restrained to be similar. Subject to these conditions, the occupancy ratio refined to 0.866(3)/0.134(3).

One pyrazole ligand (of N51 and N52) was refined as disordered. The disordered moieties were restrained to have similar geometries as another better-defined pyrazole ligand. U_{ij} components of ADPs for disordered atoms closer to each other than 2.0 Å were restrained to be similar. Subject to these conditions, the occupancy ratio refined to 0.359(5)/0.641(5).

For one of the Bu_4N^+ cations, two of the butyl chains were refined as disordered and were restrained to have similar geometries as another better-defined fragment of the same kind. The other Bu_4N^+ cation was refined as threefold disordered. The three moieties were restrained to have a similar geometry as the major moiety of the first cation. U_{ij} components of ADPs for disordered atoms closer to each other than 2.0 Å were restrained to be similar. Subject to these conditions, the occupancy ratios for the two disordered butyl chains refined to 0.778(8)/0.222(8) and 0.62(2)/0.38(2). The threefold disorder refined to 0.6269(19)/0.209(2)/0.164(2).

Extensive disorder is observed for several nitrobenzene molecules. Residue 5 and residue 8 are each twofold disordered. Residue 9 has disorder of a nitrobenzene with a pentane molecule. Five further nitrobenzene and one pentane molecule form a disordered cluster arranged around an inversion center (residues 6 and 7). One nitrobenzene molecule is disordered around the inversion center. The benzene rings of several nitrobenzene ligands were constrained to resemble ideal hexagons (AFIX 66). All nitrobenzene ligands were restrained to have similar geometries. The B moiety of residue 7 was restrained to be close to planar. The two pentane moieties were restrained to have similar geometries. U_{ij} components of ADPs for disordered atoms closer to each other than 2.0 Å were restrained to be similar. Subject to these conditions, the occupancy ratios refined to 0.802(4)/0.198(4) for residue 5 and to 0.693(4)/0.307(4) for residue 8. Occupancy ratios refined to 0.367(5) for moiety 1 of residue 6, 0.3731(19) for moiety 2 of residue 6, 0.100(4) for moiety 3 of residue 6, 0.120(10) for moiety 4 of residue 6 (a pentane molecule), 0.6269(19) for moiety 1 of residue 7, and 0.3731(19) for moiety 2 of

https://doi.org/10.1021/acs.cgd.2c01261
Cryst. Growth Des. 2023, 23, 1676−1688

residue 7. The nitrobenzene of residue 9 refined to 0.307(4) and the pentane to 0.764(5).

1b. Hydroxyl H atom positions were refined, and O−H distances were restrained to a target value of 0.84(2) Å. The BeF_4^{2-} anion was refined as twofold disordered. The two moieties were restrained to have similar geometries. U_{ij} components of ADPs for disordered atoms closer to each other than 2.0 Å were restrained to be similar. Subject to these conditions, the occupancy ratio refined to 0.690(6)/0.310(6).

One pyrazole ligand (of N53 and N54) was refined as disordered. The disordered moieties were restrained to have similar geometries as another better-defined pyrazole ligand. U_{ij} components of ADPs for disordered atoms closer to each other than 2.0 Å were restrained to be similar. Subject to these conditions, the occupancy ratio refined to 0.805(8)/0.195(8).

For both of the Bu_4N^+ cations, each one of the butyl chains was refined as disordered. They were restrained to have similar geometries as another better-defined fragment of the same kind. U_{ij} components of ADPs for disordered atoms closer to each other than 2.0 Å were restrained to be similar. Subject to these conditions, the occupancy ratio for the two disordered butyl chains refined to 0.541(12)/0.459(12) (residue 2) and 0.573(13)/0.427(13) (residue 3).

Seven sites occupied by chlorobenzene molecules or mixtures of chlorobenzene and pentane are present. All but one site (residue 4) were refined as disordered. Twofold disorder was refined for residues 5 and 6, threefold disorder for residue 9, fourfold disorder for residue 8, and threefold disorder involving two chlorobenzenes and one pentane moiety was refined for residue 10. For all but this last residue, sites were constrained to full occupancy. All chlorobenzene molecules were restrained to have similar geometries. Nine disordered chlorobenzene moieties were restrained to be close to planar. Pentane bond distances and angles were restrained to expected target values. U_{ij} components of ADPs for disordered atoms closer to each other than 2.0 Å were restrained to be similar. For residue 9, atoms were restrained to be close to isotropic. Subject to these conditions, the occupancy ratios refined to 0.850(5)/0.150(5) (residue 5), 0.779(7)/0.221(7) (residue 6), 0.396(3)/0.348(3)/0.256(3) (residue 7), 0.290(3)/0.274(3)/0.246(3)/0.189(3) (residue 8), 0.371(9)/0.259(8)/0.239(8) (residue 9), and 0.267(6)/0.238(8)/0.171(10) (residue 10).

3a. Hydroxyl H atom positions were refined, and O−H distances were restrained to 0.84(2) Å. The BeF_4^{2-} anion was refined as disordered by rotation. The three disordered moieties were restrained to have similar geometries. U_{ij} components of ADPs for disordered atoms closer to each other than 2.0 Å were restrained to be similar. All Be ions were constrained to have identical ADPs. Subject to these conditions, the occupancy ratio refined to 0.396(3)/0.286(3)/0.318(3).

The two Bu_4N^+ cations were refined as disordered. The disordered moieties were restrained to have similar geometries. U_{ij} components of ADPs for disordered atoms closer to each other than 2.0 Å were restrained to be similar. Subject to these conditions, the occupancy ratios refined to 0.506(8)/0.494(8) for the cation of residue 3, and to 0.533(6)/0.467(6) for the cation of residue 4.

All but one of the eight solvate toluene molecules were refined as disordered. All toluene moieties were restrained to have similar geometries. The ill-defined molecules of residue 9 were also restrained to be close to planar, and those of residues 8 and 9 to be close to isotropic. U_{ij} components of ADPs for all disordered toluene atoms closer to each other than 2.0 Å were restrained to be similar. Subject to these conditions, the occupancy ratios refined to 0.739(12)/0.261(12) for residue 6, to 0.822(12)/0.178(12) for residue 7, to 0.647(16)/0.353(16) for residue 8, to 0.602(15)/0.398(15) for residue 9, and to 0.678(14)/0.322(14) for residue 10.

3b. The crystal under investigation was found to be non-merohedrally twinned. The orientation matrices for the two components were identified using the program Cell_Now,[46] with the two components being related by a 180° rotation around the reciprocal axis (0 −1 1).

Integration using SAINT proved problematic due to excessive multiple overlap of reflections, resulting in large numbers of rejected reflections. Attempts were made to adjust integration parameters to avoid excessive rejections (through adjustments to integration queue size, integration box slicing and twin overlap parameters, and omission of box size optimization), which led to less but still substantial numbers of rejected reflections. With no complete data set obtainable through simultaneous integration of both twin domains, the data were instead handled as if not twinned, with only the major domain integrated, and converted into an HKLF 5-type format HKL file after integration using the "Make HKLF 5 File" routine as implemented in WinGX.[47] The twin law matrix that was used was obtained using Rotax,[48] as implemented in WinGX:

−1	0	0
0.428	0.247	−0.753
−0.428	1.247	−0.247

The Overlap R1 and R2 values used were 0.35, i.e., reflections with a discriminator function less or equal to an overlap radius of 0.35 were counted overlapped, all others as single. The discriminator function used was the "delta function on index non-integrality". No reflections were omitted. The structure was solved using direct methods with the HKLF 4-type file before correction using WinGX, and was refined using the HKLF 5-type file, resulting in a BASF value of 0.1588(8). No R_{int} value is obtainable for the HKLF 5-type file using the WinGX routine. The value from TWINABS[49] is given instead, which is available for all reflections and is based on an agreement between observed single and composite intensities and those calculated from refined unique intensities and twin fractions.

The central BeF_4^{2-} anion is disordered over two orientations. The two disordered moieties were restrained to have similar geometries. U_{ij} components of ADPs for disordered atoms closer to each other than 2.0 Å were restrained to be similar. Subject to these conditions, the occupancy ratio refined to 0.677(12)/0.323(12). Hydroxyl H atom positions were refined, and O−H distances were restrained to 0.84(2) Å. Where necessary, hydroxyl H atom positions were further restrained based on hydrogen-bonding considerations.

Two pyrazolate ligands were refined as disordered. The two disordered moieties were restrained to have similar geometries as the other not disordered pyrazolate rings. The minor moiety rings of N35 and N36 were restrained to be coplanar with the adjacent copper ions Cu18 and Cu19. N35 and N35B as well as N36 and N36B were constrained to each have identical ADPs. U_{ij} components of ADPs for disordered atoms closer to each other than 2.0 Å were restrained to be similar. The atoms of the ring of N19 were also restrained to be close to isotropic. Subject to these conditions, the occupancy ratio refined to 0.44(3)/0.56(3) for the ring of N19 and N20, and to 0.60(2)/0.40(2) for the ring of N35 and N36.

One of two Bu_4N^+ cations was refined as disordered. The two disordered moieties were restrained to have similar geometries as the other not disordered cation of the same kind. U_{ij} components of ADPs for disordered atoms closer to each other than 2.0 Å were restrained to be similar. Subject to these conditions, the occupancy ratio refined to 0.653(11)/0.347(11).

Two of the three sites occupied by bromobenzene were refined as disordered. One site was refined as twofold disordered with full occupancy for the entire site. The other was refined as fourfold disordered with partial occupancy for the entire site. All bromobenzene moieties were restrained to have similar geometries. The phenyl ring of partially occupied moieties was constrained to resemble exact hexagons with C−C bond distances of 1.39 Å. U_{ij} components of ADPs for disordered atoms closer to each other than 2.0 Å were restrained to be similar. Subject to these conditions, the occupancy ratios refined to 0.823(6)0.177(6) (molecules of Br2 and Br3), and the occupancy ratios for Br4−8 refined to 0.393(6), 0.146(7), 0.204(7) and 0.054(5).

In addition to twinning and disorder, the structure also exhibits large volume sections consisting of highly disordered solvate (tentatively resembling disordered hexane molecules). No satisfactory

https://doi.org/10.1021/acs.cgd.2c01261
Cryst. Growth Des. 2023, 23, 1676−1688

model could be developed, and the contribution of the solvate molecules was instead taken into account by reverse Fourier transform methods. The data were first detwinned (using the LIST 8 function of Shelxl2018), and then the CIF and FCF files were subjected to the SQUEEZE routine, as implemented in the program Platon.[50] The resultant files were used in further refinement. Both the HKLF 5-type HKL file and the detwinned FAB file are appended to the CIF file. A volume of 1356 Å^3 per unit cell containing 1356 electrons was corrected for.

4a. Hydroxyl H atom positions were refined, and O−H distances were restrained to a target value of 0.84(2) Å. The positions of H-atoms H3O and H29O were further restrained based on hydrogen-bonding considerations (2.10(2) Å to O35 and O32, respectively).

The SO_4^{2-} anion was refined as twofold disordered. All S−O bond distances and all O−S−O angles were restrained to be each similar to each other. U_{ij} components of ADPs for disordered atoms closer to each other than 2.0 Å were restrained to be similar. Subject to these conditions, the occupancy ratio refined to 0.419(6)/0.581(6).

One pyrazole ligand (of N36) was refined as disordered. The disordered moieties were restrained to have similar geometries as another better-defined pyrazole ligand, and Cu−N distances were restrained to be similar to each other. U_{ij} components of ADPs for disordered atoms closer to each other than 2.0 Å were restrained to be similar. Subject to these conditions, the occupancy ratio refined to 0.719(16)/0.281(16).

One of the Bu_4N^+ cations (N63) exhibits minor disorder of one butyl chain. The other exhibits whole-cation disorder. In the former, atoms C103 through C105 were refined as disordered and were restrained to have similar geometries as another better-defined fragment of the same kind. The moieties of the second cation (N64) were restrained to have similar geometries as the major moiety of the first cation. U_{ij} components of ADPs for disordered atoms closer to each other than 2.0 Å were restrained to be similar. Subject to these conditions, the occupancy ratio refined to 0.631(18)/0.369(18) for C103 through C105, and to 0.570(8)/0.430(8) for the second cation.

Chlorobenzene and pentane solvate molecules are extensively disordered. All chlorobenzene molecules as well as all pentane moieties were each restrained to have similar geometries. U_{ij} components of ADPs for disordered atoms closer to each other than 2.0 Å were restrained to be similar, and some solvate atoms were restrained to be close to isotropic. A global anti-bumping restraint was applied. Subject to these conditions, the occupancy ratios refined to the values given in the CIF file.

4b. Hydroxyl H atom positions were refined, and O−H distances were restrained to a target value of 0.84(2) Å. The position of H-atoms H4O and H21O of the first molecule and of H22O of the second molecule were further restrained, based on hydrogen-bonding considerations (2.20(2) Å to O32B_1, 2.10(2) Å to O31_1, and 2.00(2) Å to O31_2, respectively).

The two SO_4^{2-} anions were both refined as twofold disordered. Major and minor moieties were restrained to have similar geometries. U_{ij} components of ADPs for disordered atoms closer to each other than 2.0 Å were restrained to be similar. Subject to these conditions, the occupancy ratio refined to 0.687(6)/0.313(6) for sulfate 1, and to 0.721(5)/0.279(5) for sulfate 2.

For anion complex 1, four pyrazole ligands were refined as disordered (of N5, N11, N19, and N21). The pyrazole of N5/N6 is disordered in a 1:1 ratio, with one of the moieties in conflict with a half-occupied Bu_4N^+ cation (see below for details). The pyrazole of N11/N12 is disordered in a general position. The disorder of pyrazoles of N19/N20 and N21/N22 is correlated, and adjacent Cu10 and Cu11 are included in the disorder. This disorder is also correlated with solvate disorder (of the dichlorobenzene of Cl31/Cl32, Cl33/Cl34, Cl35/Cl36, and Cl27/Cl28). A common occupancy factor was used. For the pyrazoles of N5/N6 and N11/N12, the disordered moieties were restrained to have similar geometries as another better-defined pyrazole ligand (N1/N2). For the other two disordered pyrazoles and copper atoms (with the joint disorder), the geometries of major and minor moieties were restrained to be similar. U_{ij} components of ADPs for disordered atoms closer to each other than 2.0 Å were restrained to be similar. Subject to these conditions, the occupancy ratio refined to 0.417(11)/0.583(11) for N11/N12 and to 0.559(3)/0.441(3) for the joint disorder. No pyrazole disorder was observed for the second anion complex.

Disorder is observed for three of the four Bu_4N^+ cations. The cation of N63_2 is not disordered. The cation of N64_2 is disordered by whole-cation disorder in a general position (with the cation of N65_2). The three cation moieties were restrained to have similar geometries, and for the disordered cations, U_{ij} components of ADPs for atoms closer to each other than 2.0 Å were restrained to be similar. Subject to these conditions, the occupancy ratio refined to 0.618(4)/0.382(4). The cation of N63_1 exhibits disorder of one butyl chains. It was restrained to have a similar geometry as another better-defined butyl group of the same cation. U_{ij} components of ADPs for atoms closer to each other than 2.0 Å were restrained to be similar. Subject to these conditions, the occupancy ratio refined to 0.558(15)/0.442(15). The last cation is disordered around an inversion center with two symmetry independent cation positions (of N64_1 and N65_1) that partially overlap with each other. The cation of N65_1 is mutually exclusive with its symmetry-created counterpart across the inversion center, thus enforcing an exact 1:1 occupancy ratio. Both half-occupied moieties were restrained to have similar geometries, and for the disordered cations, U_{ij} components of ADPs for atoms closer to each other than 2.0 Å were restrained to be similar. The outer butyl chains that do not overlap between the cation moieties do partially overlap with disordered solvate molecules (*e.g.*, the 1,2-dichlorobenzene molecule of Cl35/Cl36) and disordered pyrazole ligands (N5/N6).

A large number of 1,2-dichlorobenzene solvate molecules are present, and the majority is extensively disordered. All 1,2-dichlorobenzene moieties were each restrained to have similar geometries. Some were restrained to be close to planar (those of Cl5/Cl6, Cl5B/Cl6B, Cl23/Cl24, Cl25/Cl26, Cl35/Cl36, Cl37/Cl38, and Cl39/Cl40). For some 1,2-dichlorobenzene molecules (mostly not disordered but ill defined), a rigid bond restraint was applied to its displacement parameters (those of Cl5/Cl6, Cl9/Cl10, Cl13/Cl14, Cl15/Cl16, Cl27/Cl28, Cl29/Cl30, and Cl37/Cl38). For disordered 1,2-dichlorobenzene molecules, U_{ij} components of ADPs for atoms closer to each other than 2.0 Å were restrained to be similar. Subject to these conditions, the occupancy ratios refined to the values given in the CIF file.

A heptane molecule was refined as disordered across an inversion center. Bond distances and angles were restrained to the expected target values. U_{ij} components of ADPs for disordered atoms closer to each other than 2.0 Å were restrained to be similar, and atoms were restrained to be close to isotropic.

The structure contains additional 3293 Å^3 of solvent-accessible voids. No substantial electron density peaks were found in the solvent-accessible voids (less than 2.5 electron per Å^3), and the residual electron density peaks were not arranged in an interpretable pattern. The structure factors were instead augmented via reverse Fourier transform methods using the SQUEEZE routine, as implemented in the program Platon. The resultant FAB file containing the structure factor contribution from the electron content of the void space was used together with the original HKL file in further refinement. The FAB file with details of the SQUEEZE results is appended to the CIF file. The SQUEEZE procedure corrected for 913 electrons within the solvent-accessible voids.

5a. Hydroxyl H atom positions were refined, and O−H distances were restrained to 0.84(2) Å. The BeF_4^{2-} anion was refined as disordered over three orientations. The disordered moieties were restrained to have similar geometries. U^{ij} components of ADPs for disordered atoms closer to each other than 2.0 Å were restrained to be similar. Subject to these conditions, the occupancy ratio refined to 0.339(4)/0.422(4)/0.239(4).

Two butyl chains of one Bu_4N^+cation were refined as disordered. For the other Bu_4N^+cation, whole-ion disorder was refined. The disordered moieties were restrained to have similar geometries as not disordered counterparts or as the major moiety of the first cation. All C−N bond lengths were restrained to be similar in length. U_{ij}

https://doi.org/10.1021/acs.cgd.2c01261
Cryst. Growth Des. 2023, 23, 1676−1688

components of ADPs for disordered atoms closer to each other than 2.0 Å were restrained to be similar. Subject to these conditions, the occupancy ratio refined to 0.592(6)/0.408(6) and 0.651(15)/0.349(15) for the disordered butyl chains, and to 0.630(7)/0.370(7) for the whole-ion disorder.

Six sites occupied by dichlorobenzene were refined. Two were refined as not disordered but partially occupied (residues 6 and 9). Two were refined as threefold disordered and fully occupied. And two were refined as disordered with a heptane molecule. All dichlorobenzene moieties were restrained to have similar geometries. Heptane C−C bonds and angles were restrained to the expected target values. The major moiety of residue 10 (disordered with the heptane) and the lowest occupancy moiety of residue 8 were restrained to be close to planar. U_{ij} components of ADPs for disordered atoms closer to each other than 2.0 Å were restrained to be similar. Non-disordered dichlorobenzene moieties were subjected to a rigid bond restraint. Subject to these conditions, the solvate occupancy ratio refined to the values listed in the atom table of the CIF file.

A global mild anti-bumping restraint was applied. The structure contains additional 1425 $Å^3$ of solvent-accessible voids. No substantial electron density peaks were found in the solvent-accessible voids (less than two electrons per $Å^3$), and the residual electron density peaks are not arranged in an interpretable pattern. The structure factors were instead augmented via reverse Fourier transform methods using the SQUEEZE routine, as implemented in the program Platon. The resultant FAB file containing the structure factor contribution from the electron content of the void space was used together with the original HKL file for further refinement. The FAB file with details of the SQUEEZE results is appended to the CIF file. The SQUEEZE procedure corrected for 334 electrons within the solvent-accessible voids.

$(Bu_4N)_3Be_2F_7(H_2O)_3$. Three of the four butyl chains were refined as disordered. The disordered moieties were restrained to have similar geometries as the one non-disordered chain. U_{ij} components of ADPs for disordered atoms closer to each other than 2.0 Å were restrained to be similar. Subject to these conditions, the occupancy ratio refined to 0.743(6)/0.257(6) (chain of C1), to 0.863(5)/0.137(5) (chain of C5; C5 and C6 omitted from disorder), and to 0.897(5)/0.103(5) (chain of C13). Distinct difference density peaks around the Be_2F_7 moiety indicate disorder. However, no meaningful disorder model could be devised, and any disorder, if present, was not modeled.

■ ASSOCIATED CONTENT

Supporting Information

The Supporting Information is available free of charge at https://pubs.acs.org/doi/10.1021/acs.cgd.2c01261.

Additional X-ray crystallographic data (PDF)

Accession Codes

CCDC 2216028−2216035 contain the supplementary crystallographic data for this paper. These data can be obtained free of charge via www.ccdc.cam.ac.uk/data_request/cif, or by emailing data_request@ccdc.cam.ac.uk, or by contacting The Cambridge Crystallographic Data Centre, 12 Union Road, Cambridge CB2 1EZ, UK; fax: +44 1223 336033.

■ AUTHOR INFORMATION

Corresponding Author

Gellert Mezei − *Department of Chemistry, Western Michigan University, Kalamazoo, Michigan 49008, United States;* orcid.org/0000-0002-3120-3084; Email: gellert.mezei@wmich.edu

Authors

Wisam A. Al Isawi − *Department of Chemistry, Western Michigan University, Kalamazoo, Michigan 49008, United States;* orcid.org/0000-0002-2900-1678

Matthias Zeller − *Department of Chemistry, Purdue University, West Lafayette, Indiana 47907, United States;* orcid.org/0000-0002-3305-852X

Complete contact information is available at: https://pubs.acs.org/10.1021/acs.cgd.2c01261

Notes

The authors declare no competing financial interest.

■ ACKNOWLEDGMENTS

This material is based on work supported by the National Science Foundation under Grant No. CHE-1808554.

■ REFERENCES

(1) Svilar, M.; Schuster, G.; Civic, T.; Sabey, P.; Vidal, E.; Freeman, S.; Petzow, G.; Aldinger, F.; Jönsson, S.; Welge, P.; Kampen, V.; Mensing, T.; Brüning, T.Ullmann's Encyclopedia of Industrial Chemistry. In *Beryllium and Beryllium Compounds*; Wiley-VCH: Weinheim, 2013; pp 1−35.

(2) Bell, N. A. Beryllium Halides and Pseudohalides. *Adv. Inorg. Chem. Radiochem.* **1972**, *14*, 255−332.

(3) Forsberg, C. The Advanced High-Temperature Reactor: High-Temperature Fuel, Liquid Salt Coolant, Liquid-Metal-Reactor Plant. *Prog. Nucl. Energy* **2005**, *47*, 32−43.

(4) Sorbom, B. N.; Ball, J.; Palmer, T. R.; Mangiarotti, F. J.; Sierchio, J. M.; Bonoli, P.; Kasten, C.; Sutherland, D. A.; Barnard, H. S.; Haakonsen, C. B.; Goh, J.; Sung, C.; Whyte, D. G. ARC: A Compact, High-Field, Fusion Nuclear Science Facility and Demonstration Power Plant with Demountable Magnets. *Fusion Eng. Des.* **2015**, *100*, 378−405.

(5) Stonehouse, A. J.Physics and Chemistry of Beryllium. https://materion.com/products/beryllium-products/beryllium-metal (accessed October 25, 2022).

(6) Naglav, D.; Buchner, M. R.; Bendt, G.; Kraus, F.; Schulz, S. Off the Beaten Track—A Hitchhiker's Guide to Beryllium Chemistry. *Angew. Chem., Int. Ed.* **2016**, *55*, 10562−10576.

(7) Groom, C. R.; Bruno, I. J.; Lightfoot, M. P.; Ward, S. C. The Cambridge Structural Database. *Acta Crystallogr., Sect. B: Struct. Sci., Cryst. Eng. Mater.* **2016**, *72*, 171−179. (accessed October 25, 2022)

(8) Al Isawi, W. A.; Zeller, M.; Mezei, G. Supramolecular Incarceration and Extraction of Tetrafluoroberyllate from Water by Nanojars. *Inorg. Chem.* **2022**, *61*, 8611−8622.

(9) Barker, T. V. CCLX. —Studies in Chemical Crystallography. Part 1. Co-ordination, Isomorphism, and Valency. *J. Chem. Soc., Trans.* **1912**, *101*, 2484−2502.

(10) Rây, P. C. Isomorphism and Homology. *Nature* **1929**, *124*, 480−481.

(11) Sarkar, P. B.; Ray, N. A Preliminary Note on the Homology of BeF_4'' and SO_4'' Ions from Chemical, Structural and Crystallographic Points of View. *J. Indian Chem. Soc.* **1929**, *6*, 987−990.

(12) Pies, W.; Weiss, A.Complex Fluorides and Fluorine Double Salts. In *Landolt-Börnstein − Group III Condensed Matter 7A (Key Elements: F, Cl, Br, I)*; Hellwege, K.-H.; Hellwege, A. M., Eds.; Springer-Verlag: Berlin/Heidelberg, 1973.

(13) Le Fur, Y.; Aléonard, S. Étude d'Orthofluorobéryllates $Me_2^{I}Me_2^{II}(BeF_4)_3$ de Structure Langbeinite. *Mater. Res. Bull.* **1969**, *4*, 601−615.

(14) Mezei, G.; Baran, P.; Raptis, R. G. Anion Encapsulation by Neutral Supramolecular Assemblies of Cyclic Cu^{II} Complexes: A Series of Five Polymerization Isomers, $[\{cis\text{-}Cu^{II}(\mu\text{-}OH)(\mu\text{-}pz)\}_n]$, n = 6, 8, 9, 12, and 14. *Angew. Chem., Int. Ed.* **2004**, *43*, 574−577.

(15) Fernando, I. R.; Surmann, S. A.; Urech, A. A.; Poulsen, A. M.; Mezei, G. Selective Total Encapsulation of the Sulfate Anion by Neutral Nano-Jars. *Chem. Commun.* **2012**, *48*, 6860−6862.
(16) Ahmed, B. M.; Szymczyna, B. R.; Jianrattanasawat, S.; Surmann, S. A.; Mezei, G. Survival of the Fittest Nanojar: Stepwise Breakdown of Polydisperse Cu_{27}−Cu_{31} Nanojar Mixtures into Monodisperse $Cu_{27}(CO_3)$ and $Cu_{31}(SO_4)$ Nanojars. *Chem. − Eur. J.* **2016**, *22*, 5499−5503.
(17) Ahmed, B. M.; Hartman, C. K.; Mezei, G. Sulfate-Incarcerating Nanojars: Solution and Solid-State Studies, Sulfate Extraction from Water, and Anion Exchange with Carbonate. *Inorg. Chem.* **2016**, *55*, 10666−10679.
(18) Al Isawi, W. A.; Zeller, M.; Mezei, G. Tribenzyl(methyl)-ammonium: A Versatile Counterion for the Crystallization of Nanojars with Incarcerated Selenite and Phosphite Ions and Tethered Pyrazole Ligands. *Cryst. Growth Des.* **2022**, *22*, 1398−1411.
(19) Al Isawi, W. A.; Salome, A. Z.; Ahmed, B. M.; Zeller, M.; Mezei, G. Selective Binding of Anions by Rigidified Nanojars: Sulfate vs. Carbonate. *Org. Biomol. Chem.* **2021**, *19*, 7641−7654.
(20) Aléonard, S.; Gorius, M.-F. Structure Cristalline du Pyrofluorobéryllate de Guanidinium $(CN_3H_6)_3Be_2F_7$. *C. R. Acad. Sci. Paris, Ser. II* **1989**, *309*, 683−687.
(21) Neumüller, B.; Dehnicke, K. Hexafluorodiberyllate, $[Be_2F_6]^{2-}$. Synthesis and Crystal Structure of $(Ph_4P)_4[Be_2F_6][SiF_6]\cdot 6CH_3CN$. *Z. Anorg. Allg. Chem.* **2005**, *631*, 2535−2537.
(22) Tonner, R.; Frenking, G.; Neumüller, B.; Dehnicke, K. $(Ph_4P)_2[Be_2F_6]\cdot 2CH_3CN$: Synthesis, IR Spectra, Crystal Structure, and Quantum Chemical Calculations. *Z. Anorg. Allg. Chem.* **2007**, *633*, 1183−1188.
(23) Boldog, I.; Daran, J.-C.; Chernega, A. N.; Rusanov, E. B.; Krautscheid, H.; Domasevitch, K. V. Hydrogen Bonding Patterns and Supramolecular Structure of 4,4′-Bipyrazolium Salts. *Cryst. Growth Des.* **2009**, *9*, 2895−2905.
(24) De Vries, K. J.; Gellings, P. J. The Thermal Decomposition of Potassium and Sodium Pyrosulfate. *J. Inorg. Nucl. Chem.* **1969**, *31*, 1307−1313.
(25) Hofmeister, H. K.; Van Wazer, J. R. Hydrolysis of Sodium Pyrosulfate. *Inorg. Chem.* **1962**, *1*, 811−812.
(26) Chen, S.-Q.; Zhao, W.; Wu, B. Separation of Sulfate Anion from Aqueous Solution Governed by Recognition Chemistry: A Minireview. *Front. Chem.* **2022**, *10*, No. 905563.
(27) Ravikumar, I.; Ghosh, P. Recognition and Separation of Sulfate Anions. *Chem. Soc. Rev.* **2012**, *41*, 3077−3098.
(28) Šoptrajanov, B.; Trpkovska, M.; Zdravkovski, Z. Tetrafluoroberyllate(2−) Ions as Hydrogen-Bond Proton Acceptors: Spectroscopic Evidence. *Spectrosc. Lett.* **1996**, *29*, 867−875.
(29) Pejov, L.; Trpkovska, M.; Šoptrajanov, B. Tetrafluoroberrylate-(2−) Ions as Hydrogen-Bond Proton Acceptors: Quantum Chemical Considerations. *Spectrosc. Lett.* **1999**, *32*, 361−369.
(30) Robinson, E. A.; Johnson, S. A.; Tang, T.-H.; Gillespie, R. J. Reinterpretation of the Lengths of Bonds to Fluorine in Terms of an Almost Ionic Model. *Inorg. Chem.* **1997**, *36*, 3022−3030.
(31) Cannon, W. R.; Montgomery Pettitt, B.; McCammon, J. A. Sulfate Anion in Water: Model Structural, Thermodynamic, and Dynamic Properties. *J. Phys. Chem. A* **1994**, *98*, 6225−6230.
(32) Smeeton, L. C.; Farrell, J. D.; Oakley, M. T.; Wales, D. J.; Johnston, R. L. Structures and Energy Landscapes of Hydrated Sulfate Clusters. *J. Chem. Theory Comput.* **2015**, *11*, 2377−2384.
(33) Umesaki, N.; Iwamoto, N.; Ohno, H.; Furukawa, K. Structural Analysis of Molten Na_2BeF_4 and $NaBeF_3$ by X-ray Diffraction. *J. Chem. Soc., Faraday Trans. 1* **1982**, *78*, 2051−2058.
(34) Weikert, H.-G.; Cederbaum, L. S. Free Doubly Negative Tetrahalides. *J. Chem. Phys.* **1993**, *99*, 8877−8891.
(35) Middleton, R.; Klein, J. Experimental Verification of the Existence of the Gas-Phase Dianions BeF_4^{2-} and MgF_4^{2-}. *Phys. Rev. A* **1999**, *60*, 3515−3521.
(36) Feeney, J.; Haque, R.; Reeves, L. W.; Yue, C. P. Nuclear Spin−Spin Coupling Constants; Equilibrium and Kinetic Studies for Fluoroberyllate Complexes in Solution. *Can. J. Chem.* **1968**, *46*, 1389−1398.
(37) Hogben, M. G.; Radley, K.; Reeves, L. W. Studies of Fluoroberyllate Complexes in Aqueous Solution by ^{19}F Nuclear Magnetic Resonance. *Can. J. Chem.* **1970**, *48*, 2960−2964.
(38) Schmidt, M.; Schmidbaur, H. Ligand Redistribution Equilibria in Aqueous Fluoroberyllate Solutions. *Z. Naturforsch., B: Chem. Sci.* **1998**, *53*, 1294−1300.
(39) Al Isawi, W. A.; Ahmed, B. M.; Hartman, C. K.; Seybold, A. N.; Mezei, G. Are Nanojars Unique to Copper? Solution and Solid State Characterization of High-Symmetry Octanuclear Nickel(II)-Pyrazolate Complexes. *Inorg. Chim. Acta* **2018**, *475*, 65−72.
(40) (a) *Bruker APEX3*.Bruker AXS Inc.: Madison, Wisconsin, USA, 2016. (b) *Bruker APEX4*.Bruker AXS Inc.: Madison, Wisconsin, USA, 2022.
(41) *Bruker SAINT v.8.38A*.Bruker: Madison, Wisconsin, USA, 2017.
(42) Krause, L.; Herbst-Irmer, R.; Sheldrick, G. M.; Stalke, D. Comparison of Silver and Molybdenum Microfocus X-Ray Sources for Single-Crystal Structure Determination. *J. Appl. Crystallogr.* **2015**, *48*, 3−10.
(43) Sheldrick, G. M. A Short History of SHELX. *Acta Crystallogr., Sect. A: Found. Crystallogr.* **2008**, *64*, 112−122.
(44) Sheldrick, G. M. SHELXT − Integrated Space-Group and Crystal-Structure Determination. *Acta Crystallogr., Sect. A: Found. Crystallogr.* **2015**, *A71*, 3−8.
(45) Sheldrick, G. M. Crystal Structure Refinement with SHELXL. *Acta Crystallogr., Sect. C: Struct. Chem.* **2015**, *C71*, 3−8.
(46) Sheldrick, G. M.*CELL_NOW. Version 2008/4*; University of Göttingen: Germany, 2008.
(47) Farrugia, L. J. WinGX and ORTEP for Windows: An Update. *J. Appl. Crystallogr.* **2012**, *45*, 849−854.
(48) Cooper, R. I.; Gould, R. O.; Parsons, S.; Watkin, D. J. The Derivation of Non-Merohedral Twin Laws During Refinement by Analysis of Poorly Fitting Intensity Data and the Refinement of Non-Merohedrally Twinned Crystal Structures in the Program CRYSTALS. *J. Appl. Crystallogr.* **2002**, *35*, 168−174.
(49) Sheldrick, G. M.*TWINABS 2012/1*; Bruker: Madison, Wisconsin, USA.
(50) Spek, A. L. PLATON SQUEEZE: A Tool for the Calculation of the Disordered Solvent Contribution to the Calculated Structure Factors. *Acta Crystallogr., Sect. C: Struct. Chem.* **2015**, *71*, 9−18.

https://doi.org/10.1021/acs.cgd.2c01261
Cryst. Growth Des. 2023, 23, 1676−1688